J. Fluid Mech. (1983), *vol.* 128, *pp.* 199–217
Printed in Great Britain

Calculation of fully developed turbulent flows in ducts of arbitrary cross-section

By A. NAKAYAMA,† W. L. CHOW
Department of Mechanical and Industrial Engineering, University of Illinois at Urbana-Champaign, Urbana, IL 61801

AND D. SHARMA
Dames and Moore, Golden, CO 80401

(Received 9 October 1981 and in revised form 2 August 1982)

The algebraic stress model developed by Launder & Ying for the secondary flow of the second kind was employed with the k and ϵ model for the prediction of fully developed turbulent flows in square, rectangular and trapezoidal ducts using the numerical procedure designed for ducts of arbitrary cross-sectional shape. Results of the calculation are compared extensively with available experimental data, with strong emphasis on the local structures of turbulence to reveal full features of this particular stress model.

1. Introduction

It has been known since the experimental work of Nikuradse (1926, 1930) that a transverse mean flow exists within non-circular ducts even when the flow is fully developed. The secondary flow of this type, termed by Prandtl the secondary flow of the second kind, is attributable to the presence of Reynolds-stress gradients across the cross-sectional plane. Although the secondary flow of this kind usually amounts to a few per cent of the bulk velocity and is usually negligible if the motion is also induced by a cross-sectional pressure gradient, its presence displaces the lines of constant axial velocity (i.e. isovels) considerably toward the corners of the duct, yielding a relatively high velocity field there. Thus suppression of the secondary-flow motion in the simulation of turbulence leads to an unrealistic interpretation of the phenomenon. Any attempt to deal with this class of flow must pay special attention to the simulation of this secondary-flow motion.

The effective-viscosity formulation cannot predict the secondary flow induced by the turbulent stress field since the stress and mean-strain fields under such a formulation are coaligned. The first successful attempt to predict the fully developed flow in a square duct was made by Launder & Ying (1973) with a one-equation model coupled to the 'algebraic stress model'. They demonstrated that the mean velocity field can be predicted fairly well by their algebraic stress model. However, no comparison of the computation and the experiment was made on the individual Reynolds-stress components. Their innovative numerical work on the secondary-flow prediction was followed by several studies to calculate the fully developed flows in some other non-circular geometries; for example those of Aly, Trupp & Gerrard (1978)

† Present address: Department of Mechanical Engineering, Shizuoka University, Hamamatsu, Japan.

and Gosman & Rapley (1978) for an equilateral triangular duct and Carajilescov & Todreas (1975) for triangular rod bundles. This algebraic stress model was effective for prediction of the mean-flow quantities. None of these studies revealed the details of the model performance on the local structures of turbulence.

Even when dealing with more complicated non-circular geometries, it is still possible to retain the Cartesian or cylindrical polar coordinate system. When using such systems, however, one must do extensive interpolative calculations in order to satisfy the required boundary conditions. Moreover, a considerable number of mesh points will be wasted since the points external to the flow field do not participate in the calculations in any meaningful manner. To overcome this problem in the calculations for non-circular ducts, Gosman & Rapley (1978, 1980) employed a curvilinear mesh system which is itself generated numerically.

This paper describes a general numerical scheme for prediction of the fully developed turbulent flows in ducts of arbitrary cross-section. The method employs the algebraic stress model along with the two-equation (k and ϵ) model; thereby their capability for describing the secondary flow effects can be explored. In order to achieve maximum generality in practical applications, a general procedure for the non-orthogonal coordinate transformation was developed and implemented in the computational scheme.

Calculations were performed on square, rectangular† and trapezoidal ducts and the results are compared with available experimental data. Discussions following the theoretical development are intended to reveal the full features of this particular stress model with strong emphasis on the local structures of turbulence which were neglected in most of the previous numerical studies. Special attention is directed to the predicted contour maps of the quantities responsible for the secondary-flow generation, such as the anistropy of normal stresses and the secondary shear stress working on the cross-sectional plane. No other systematic discussions of the contours of these important turbulence quantities (through the comparison of the experiment and the prediction) seem to have been reported elsewhere. The discussions extend further to the kinetic-energy balance on the cross-sectional plane. This energy-balance consideration is made by comparing the contour maps of the individual terms in the turbulent kinetic-energy transport equation. It is hoped that the present report will provide information needed for further improvements of this algebraic stress model.

The results reported here are based on a part of the doctoral thesis of the first author (Nakayama 1981), which presented a series of comparisons between available experimental data and predictions of the three-dimensional version of the present numerical scheme including the three-dimensional developing turbulent flow in a square duct and also the three-dimensional turbulent separated flow in a rectangular diffuser. Other details not included in this paper may be found elsewhere (Nakayama 1981; Nakayama, Chow & Sharma 1981).

2. Theoretical development

2.1. *Governing equations and turbulence model*

Upon choosing the x-coordinate in the axial direction for the fully developed flows, the general conservation equation may be given in Cartesian coordinates (x, y, z) as

$$(v\phi - \Gamma\phi_y)_y + (w\phi - \Gamma\phi_z)_z = s_\phi, \tag{1}$$

† For the square and rectangular ducts, the coordinate transformation is not really necessary.

where u, v and w are the mean-velocity components in the x-, y- and z-directions respectively. The subscripts x, y and z denote partial derivatives.

The general dependent variable ϕ stands for any one of the dependent variables under consideration, Γ is the corresponding diffusion coefficient and s_ϕ denotes any source term. Equation (1) may be regarded as a general form common to all governing equations, namely the continuity equation, the u-, v- and w-momentum equations, and the scalar conservation equations such as the transport equations for the turbulent kinetic energy k and its rate of dissipation ϵ.

The diffusion coefficient Γ and the source term s_ϕ in Cartesian form are listed below for each governing equation:
for the continuity equation

$$\phi = 1, \quad \Gamma = 0, \quad s_\phi = 0; \tag{2a}$$

for the u-momentum equation

$$\phi = u, \quad \Gamma = \nu + \nu_t, \quad s_\phi = -\frac{p_x}{\rho}; \tag{2b}$$

for the v-momentum equation

$$\phi = v, \quad \Gamma = \nu, \quad s_\phi = -\frac{(p-\tau_{yy})_y}{\rho} + \frac{(\tau_{yz})_z}{\rho}; \tag{2c}$$

for the w-momentum equation

$$\phi = w, \quad \Gamma = \nu, \quad s_\phi = -\frac{(p-\tau_{zz})_z}{\rho} + \frac{(\tau_{yz})_y}{\rho}; \tag{2d}$$

for the equation of turbulent kinetic energy

$$\phi = k, \quad \Gamma = \nu + \frac{\nu_t}{\sigma_k}, \quad s_\phi = P - \epsilon; \tag{2e}$$

for the equation of the dissipation rate

$$\phi = \epsilon, \quad \Gamma = \nu + \frac{\nu_t}{\sigma_\epsilon}, \quad s_\phi = \frac{(c_1 P - c_2 \epsilon)\epsilon}{k}. \tag{2f}$$

In the above equations, ρ and p denote density and pressure, P is the production rate of kinetic energy, and c_1 and c_2 are empirical constants; σ_k and σ_ϵ, the effective Prandtl numbers of k and ϵ, have been introduced. ν is the kinematic viscosity, while the turbulent kinematic viscosity is denoted by ν_t, which is related to k and ϵ through the near-wall constant c_D as

$$\nu_t = c_D k^2/\epsilon. \tag{3}$$

The algebraic stress model originally developed by Launder & Ying (1973) was later evolved into explicit expressions for all six Reynolds-stress components by Gessner & Emery (1976). This explicit set is given as follows:

$$\frac{\tau_{xx}}{\rho} = -c'_{k0} k, \quad \frac{\tau_{xy}}{\rho} = \nu_t u_y, \quad \frac{\tau_{zx}}{\rho} = \nu_t u_z, \tag{4a, b, c}$$

$$\frac{\tau_{yy}}{\rho} = \frac{c' c_D k^3}{\epsilon^2} u_y^2 - c'_k k, \tag{4d}$$

$$\frac{\tau_{zz}}{\rho} = \frac{c' c_D k^3}{\epsilon^2} u_z^2 - c'_k k, \tag{4e}$$

$$\frac{\tau_{yz}}{\rho} = \frac{c' c_D k^3}{\epsilon^2} u_y u_z, \tag{4f}$$

where the empirical constants c'_{k0}, c'_k, c' and c_D are algebraically related to one another through two independent constants, which can be arbitrarily chosen among

themselves (for details see Nakayama 1981). Now the rate of production may be calculated as

$$P \approx (\tau_{xy} u_y + \tau_{zx} u_z)/\rho = \nu_t (u_y^2 + u_z^2). \tag{5}$$

The general conservation equation (1), along with (2)–(5), gives a complete set of partial differential equations under consideration. As already indicated, these governing equations have been transformed into an arbitrary system of coordinates through vector analysis. A brief discussion on this transformation procedure is given in the appendix, where the transformed version of the general conservation equation (1) may be found.

2.2. *Method of calculation*

It should be noted that the u-momentum equation may be regarded simply as another scalar conservation equation similar to that for k and ϵ, provided that the pressure-gradient term p_x is to be estimated beforehand at each iteration. In fact, experimental evidence (Leutheusser 1963) indicated that the pressure variation is very small across the cross-sectional plane.† This fact justifies the practice of estimating p_x through spatially averaging the wall shear over the cross-sectional plane, namely

$$-p_x = \frac{4\tau_{\mathrm{av}}}{D_{\mathrm{h}}} = 4\rho \frac{c_{\mathrm{D}}^{\frac{1}{2}} k_{\mathrm{av}}}{D_{\mathrm{h}}}, \tag{6}$$

where D_{h} is the hydraulic diameter and τ_{av} is the mean wall shear, which is related to the mean value of kinetic energy in the 'near-wall' region k_{av} (averaged over the periphery) through the local equilibrium relationship. Thus one needs only two-dimensional storage in computations since the x-coordinate is now completely eliminated from the governing equations.

Discretization was performed by integrating the general conservation equation over a grid volume in the transformed coordinates with non-uniform grid spacings. Following the procedure similar to the one employed by Patankar & Spalding (1972), the continuity equation is reformulated as a pressure-correction equation by substituting an abbreviated momentum balance relationship (for details of discretization procedure see Nakayama 1981).

Calculation starts with solving the v- and w-momentum equations, and subsequently this estimated cross-flow velocity field is corrected by solving the pressure-correction equation so that the velocity field fulfils the continuity principle. With p_x estimated through (6), the u-momentum equation is solved next. Finally, the turbulence quantities k and ϵ are solved. This iteration scheme also allows the variables to be updated sequentially. This iteration sequence is repeated until convergence is achieved. Convergence was measured in terms of the maximum change in each variable during an iteration. The maximum change allowed for the convergence check was 10^{-6}, when the duct width D_{n} and the bulk velocity u_{B} are chosen as the reference quantities.

Usual wall functions based on the constant-stress layer were applied to grid nodes next to the wall to match the interior flow with the required wall conditions. This practice precludes the need for fine meshes, which would otherwise be necessary to resolve steep gradients within the wall region.

† This point, actually, has been substantiated through calculations of the fully developed flow in a square duct by allowing the pressure to vary in the three-dimensional space (see Nakayama 1981). It should also be noted that, if the cross-sectional pressure gradients were considerable, the secondary motions would have to be governed by the pressure field (i.e. the secondary flow of the first kind) rather than the Reynolds-stress field (second kind).

Throughout the present study, a single set of empirical constants was used. These values are given by

$$c_D = 0{\cdot}09, \quad c'_{k0} = 0{\cdot}915, \quad c'_k = 0{\cdot}552, \quad c' = 0{\cdot}0185,$$
$$c_1 = 1{\cdot}44, \quad c_2 = 1{\cdot}92, \quad \sigma_k = 0{\cdot}9, \quad \sigma_\epsilon = 1{\cdot}3,$$
$$\kappa = 0{\cdot}41, \quad B = 5{\cdot}0,$$

where κ and B are the von Kármán constant and the wall-law intercept respectively.

Prior to the turbulent-flow calculations, extensive test calculations were performed on the various laminar-flow cases, which include the fully developed flows in square and triangular ducts as well as the laminar separated flow in a constricted circular tube. Some of these laminar-flow-calculation results were compared with the exact solutions, and others with the available numerical solutions. Thus the numerical accuracy without the presence of ambiguity due to imperfection of the turbulence modelling has been indirectly checked by different means. The discussions on these test calculations may be found elsewhere (Nakayama 1981).

3. Fully developed flow in a square duct

For the study of local flow structure it is expedient to start with a simple geometry. For this reason, the study of a square duct was conducted. Extensive discussions on the model performance follow, especially on the local turbulence fields in a square cross-section. Calculations were performed with the grid system (15×15) for the quadrant of a square at the Reynolds number (based on D_h and the bulk velocity u_B) $Re = 83000$, for which extensive measurements were carried out by Leutheusser (1963) and later reproduced by Brundrett & Baines (1964) using the same set-up.

3.1. *Mean-velocity field in a square duct*

Isovels (u/u_B) in a square duct are shown in figure 1 (*a*), where the predicted velocity levels are in good agreement with the experimental data despite the fact that distortions of contours are overestimated and the velocity near to the corner is underestimated. The discrepancy observed here, however, is consistent with the underestimation of the secondary-flow magnitude along the diagonal of the square (directed toward the corner) and also its overestimation along the wall bisector (directed toward the core). This is shown in figure 2, where the reference velocity for the secondary-flow magnitude u_{s_t} is taken as the mean wall friction velocity $u_\tau = (\tau_{av}/\rho)^{\frac{1}{2}}$, and y is the vertical coordinate with the origin at the duct centre.

The predicted secondary-flow velocity vectors and streamlines (normalized by D_h and the centreline velocity u_c) are indicated in figure 1 (*b*, *c*) along with the streamlines obtained experimentally by Gessner & Jones (1965) for $Re = 150000$ (no experimental streamline plots are available for $Re = 83000$). Even though there is experimental evidence (Gessner & Jones 1965) that the secondary-flow magnitude increases for a lower Reynolds number, the secondary-flow rate predicted here is considerably higher than that of the experimental data. At the same time, the prediction shows that the secondary motion spreads throughout the duct, while experiment indicated that the motion is somewhat concentrated near the corner. However, as noted by Gessner & Jones, their experimental data failed to satisfy the continuity principle with about 20 % error.

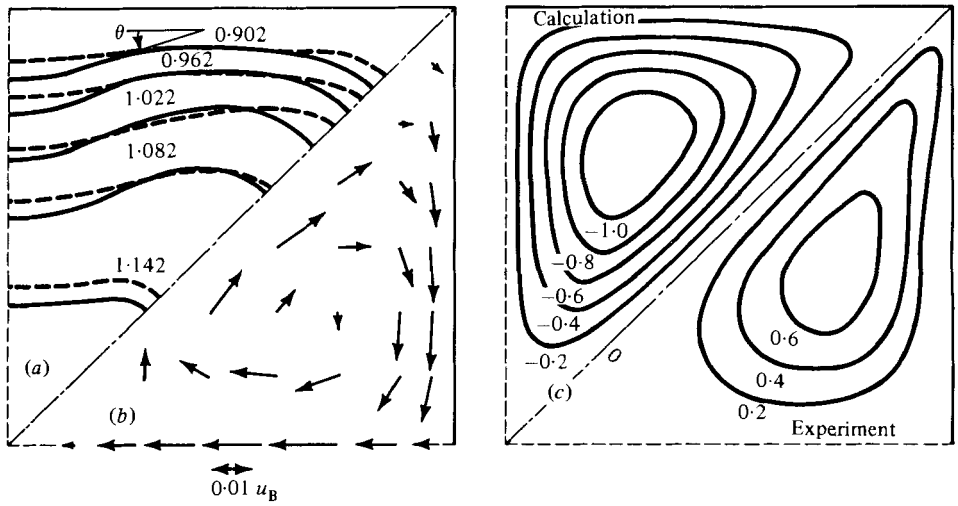

FIGURE 1. Mean-velocity field, square duct. (*a*) Isovels, u/u_B, $Re = 83000$: ——, experiment (Leutheusser 1963); – –, present calculation. (*b*) Secondary-flow vectors, present calculation, $Re = 83000$. (*c*) Secondary-flow streamlines, $(\psi/u_c D_h) \times 10^3$. Upper triangle, present calculation, $Re = 83000$; lower triangle, experiment (Gessner & Jones 1965), $Re = 150000$.

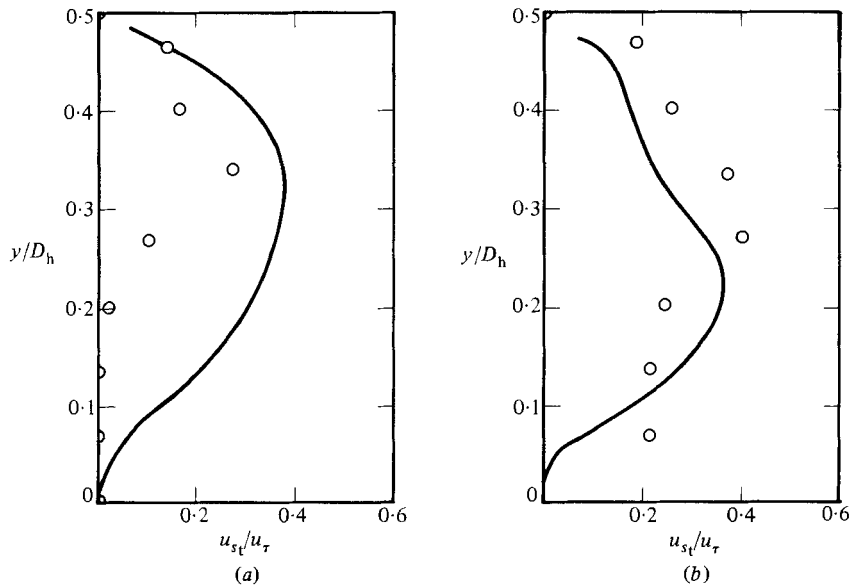

FIGURE 2. Secondary-flow velocity magnitude, u_{st}/u_τ, square duct, $Re = 83000$: ○, experiment (Brundrett & Baines, 1964); —, present calculation. (*a*) Wall bisector. (*b*) Corner bisector.

3.2. *Turbulence structures in a square duct*

3.2.1. *Kinetic energy and stresses in the axial direction.* The contour map of kinetic energy is shown in figure 3 (*a*) along with Brundrett & Baines' (1964) data (their stress data were normalized by $\frac{1}{2}\tau_{av}$ – see the discussion by Melling & Whitelaw 1976). The predicted level of kinetic energy was found to be higher than that of the experiment. The contrast between the prediction and the experiment is especially evident near the corner. This is consistent with the underprediction of the secondary-flow velocity along the diagonal, since the dilution process near the corner due to the secondary-flow

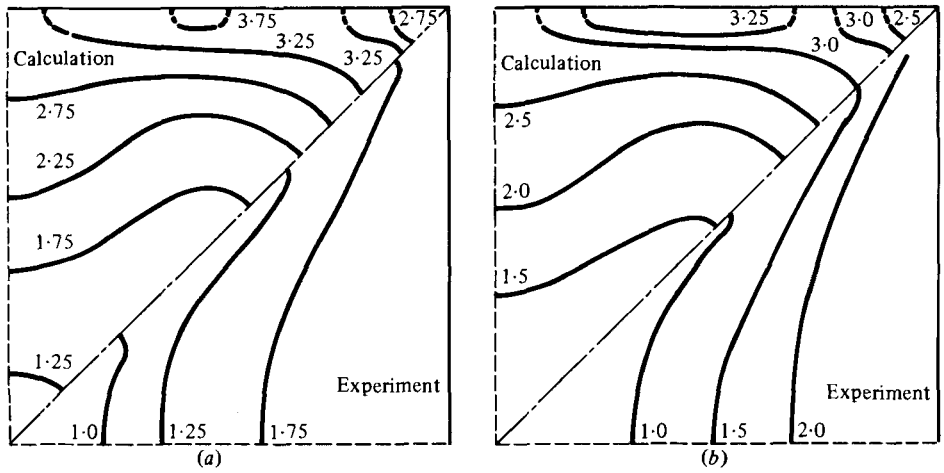

FIGURE 3. Kinetic energy and normal stress τ_{xx}, square duct $Re = 83000$. (*a*) k/u_τ; upper triangle, present calculation; lower triangle, experiment (Brundrett & Baines 1964). (*b*) $-\tau_{xx}/\tau_{av}$; upper triangle, present calculation; lower triangle, experiment (Brundrett & Baines 1964).

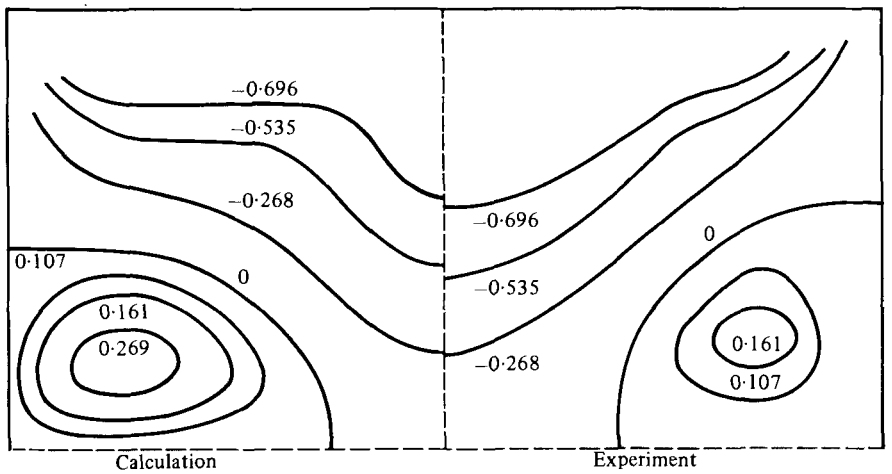

FIGURE 4. Shear stress τ_{xy}/τ_{av}, square duct: left half, present calculation, $Re = 83000$; right half, experiment (Melling & Whitelaw 1976), $Re = 42000$.

current, which carries the fluid of low kinetic energy at the core toward the corner, becomes less efficient for a lower secondary-flow velocity. The prediction and the experiment, however, share the fact that distortions of kinetic energy contours are more pronounced than those of the isovels.

Essentially the same comments as given above for the kinetic-energy contours may be made for the contour map of normal stress in the axial direction τ_{xx}, as shown in figure 3 (*b*). The shear stress opposing the primary flow τ_{xy} is shown in figure 4 along with the experimental data obtained at $Re = 42000$ by Melling & Whitelaw (1976) (contours of τ_{xy} and τ_{yy} are not available in the paper by Brundrett & Baines 1964). It should be noted that these turbulence quantities when normalized by τ_{av} become fairly insensitive to Reynolds numbers. Equations (4*b*, *c*), consistent with the effective-viscosity formulation, give the correct sign change in the shear field, and the predicted contours appear to be in good agreement with the experiment.

3.2.2. *Stresses in the cross-sectional plane.* The normal stress τ_{yy} in the cross-sectional

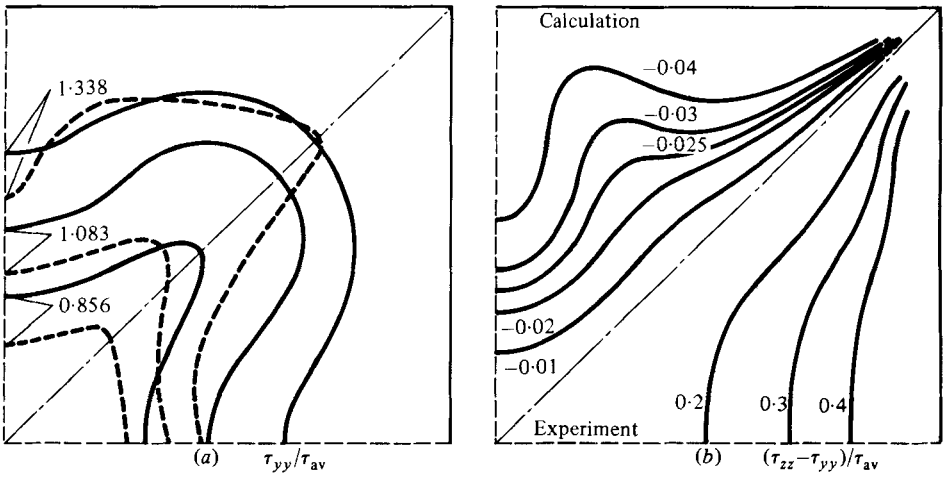

FIGURE 5. Anisotropy of normal stresses, square duct. (*a*) Normal stress, ---, experiment (Melling & Whitelaw 1976), $Re = 42000$; —, present calculation, $Re = 83000$. (*b*) $(\tau_{zz}-\tau_{yy})/\tau_{av}$, $Re = 83000$: upper triangle, present calculation; lower triangle, experiment (Brundrett & Baines 1964).

plane is indicated in figure 5(*a*) along with the experimental data obtained by Melling & Whitelaw (1976). Owing to the geometrical symmetry of a square duct, this figure may also be taken as a τ_{zz} contour map when it is rotated by $\frac{1}{2}\pi$. In other words, the lower half below the diagonal of the square may be interpreted as a τ_{zz} contour map, which would be drawn on the other half above the diagonal. Therefore the anisotropy of normal stress components $\tau_{zz}-\tau_{yy}$ can be observed from this figure through its asymmetry with respect to the diagonal. A careful observation of the predicted contours reveals the anisotropy of normal stresses, but the degree of the anisotropy is much lower than that observed in the experiment.

This fact can be seen directly from figure 5(*b*), where the predicted contours of $\tau_{zz}-\tau_{yy}$ are plotted along with Brundrett & Baines' (1964) experimental data. As indicated in the figure, the level of the predicted contours is one order less than that of the experiment. This discrepancy seems to be inherent to this particular algebraic stress model. This point is discussed in detail below.

From the transformation relations, it can readily be shown that

$$\frac{u_y}{|\nabla u|} = -\cos\theta, \quad \frac{u_z}{|\nabla u|} = \sin\theta, \tag{7}$$

$$|\nabla u| = (u_y^2 + u_z^2)^{\frac{1}{2}}, \tag{8}$$

where θ is the local angle between the tangent of the isovel and z-axis as indicated in figure 1(*a*). On the other hand, (3) and (5) under the local equilibrium condition lead to

$$\epsilon \approx P = \nu_t |\nabla u|^2 = c_D \frac{k^2}{\epsilon} |\nabla u|^2. \tag{9}$$

Therefore

$$\epsilon/k = c_D^{\frac{1}{2}} |\nabla u|. \tag{10}$$

Upon substituting (7) and (8) into (4*d–f*), one obtains the following approximate expressions, which are valid throughout the duct except at the region close to the duct centre:

$$\frac{\tau_{zz}-\tau_{yy}}{\rho k} = -c' \cos 2\theta, \tag{11}$$

$$\frac{\tau_{yz}}{\rho k} = -\tfrac{1}{2}c' \sin 2\theta. \tag{12}$$

Especially along the wall bisectors, (11) gives

$$\frac{|\tau_{zz}-\tau_{yy}|}{\rho k} = c'. \tag{13}$$

The level of the anisotropy coefficient c' obtained through (13) on the basis of the experimental data of Brundrett & Baines (1964) and Melling & Whitelaw (1976) is about 0·2, which is one order of magnitude higher than the value 0·0185 suggested by Launder & Ying (1973) and used throughout the present study (for details see Nakayama 1981). The fact, as indicated by Launder (1976), is that the model was designed and tuned on the basis of the simple yet accurate prediction of mean-flow quantities at the expense of the loss of accuracy in some of the turbulence structures, namely the quantities directly associated with c'. The paradox here is that a larger c' leads to a higher and more realistic degree of anisotropy of normal stresses, but at the same time leads to the amplification of secondary-flow motion and consequently to far more overdistorted isovels.

The curvature change of the predicted contours observed in the middle of the upper triangular section as shown in figure 5(*b*) is more significant than that of the experiment. A curvature change of this kind will be found in all the predicted $\tau_{zz}-\tau_{yy}$ contours of a non-circular duct, and again seems to be inherent to the model in which the Reynolds-stress field is directly related to the mean-strain field in a manner described by (11) and (12). This fact may be appreciated through re-examination of the figure in conjunction with the isovels in figure 1(*a*).

As indicated in (11), the relative magnitude of the anisotropy along a particular isovel is essentially determined by the local angle through $-\cos 2\theta$, since a nearly uniform wall shear stress (kinetic energy) layer exists along the wall except in the proximity of the corner as a result of secondary flow motion. When the predicted isovel nearest to the upper wall in figure 1(*a*) is traced counterclockwise from a point on the diagonal to that on the wall bisector, $-\cos 2\theta$ may be found along the isovel to vary according to

$$\langle -\cos(-\tfrac{1}{2}\pi) = 0\rangle \rightarrow \langle -\cos 0 = -1\rangle \rightarrow \langle -\cos 2\theta_{\mathrm{i}} \approx -1+2\theta_{\mathrm{i}}^2\rangle \rightarrow \langle -\cos 0 = -1\rangle,$$

where θ_{i} is the angle at the inflexion point of the isovel. The dip resulting from $2\theta_{\mathrm{i}}^2$ reflected on the contour map of the anisotropy can be appreciated from the fact that the bulge on an anisotropy contour takes place around the inflexion point on the isovel, as can be seen when figure 5(*b*) is superimposed upon figure 1(*a*).

The predicted τ_{yz} field is indicated along with the experimental value in figure 6, where the consistent difference in the order of magnitude can be seen. Moreover, the shear stress of opposite sign, although relatively small in magnitude, appears within a triangular sector. This may also be explained in the same way as presented previously for the anisotropy contours. According to (12), the shear stress τ_{yz} is essentially governed by $-\sin 2\theta$, which varies along the isovel in the counterclockwise direction as

$$\langle -\sin(-\tfrac{1}{2}\pi) = 1\rangle \rightarrow \langle -\sin 0 = 0\rangle \rightarrow \langle -\sin 2\theta_{\mathrm{i}} \approx -2\theta_{\mathrm{i}}\rangle \rightarrow \langle -\sin 0 = 0.\rangle$$

Therefore the region of opposite shear stress is to be centred around the inflexion point of the isovel. It is not clear whether such a region really exists or whether its existence is a result of the imperfection of the turbulence model. The only available experimental results on τ_{yz} contours (Brundrett & Baines 1964), however, do not indicate the existence of such a region within a lower triangular sector as shown in figure 6.

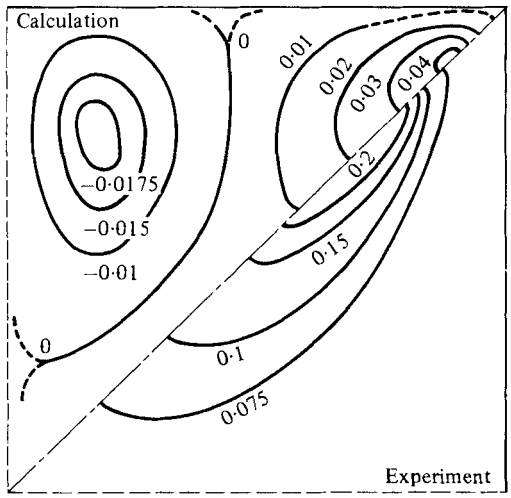

FIGURE 6. Shear stress τ_{yz}/τ_{av}, square duct, $Re = 83000$: upper triangle, present calculation; lower triangle, experiment (Brundrett & Baines 1964).

3.3. *Stress field and isovels in a square duct*

The discussion in §3.2 has been directed to the turbulence quantities $\tau_{zz}-\tau_{yy}$ and τ_{yz} (no previous studies seem to have investigated the model performance in terms of the contour maps of $\tau_{zz}-\tau_{yy}$ and τ_{yz}). The cross-sectional gradients of these quantities are primarily responsible for the secondary-flow generation, as may be observed in the vorticity-transport equation. Even though the mean-velocity field is predicted well by the algebraic stress model, the model fails to give a satisfactory agreement between prediction and experiment for these turbulence quantities associated with the secondary-flow generation.

It is not an easy task to analyse the behaviour of the stress model and eventually to improve it, since the model is based on many proposals and assumptions. Launder (1976) suggested a possible modification for the expression of the pressure–strain relationship (i.e. the redistribution term) to describe the turbulence structure in the proximity of the duct corner which possibly governs the secondary-flow generation mechanism.

On the other hand, as observed in the present study from the observation of the turbulence field in connection with the isovels, some defects in the present stress model seem to stem directly from the assumption originally implied by Prandtl (1926), namely 'the principal planes of the stress field are normal and tangent to the isovel, and the velocity fluctuations tangential to the isovel (which are greater than the normal velocity fluctuations) cause a transverse mean flow directed from the concave towards the convex side of the isovel'. Equations (11) and (12) may be regarded as a quantitiative representation of the assumption stated above (note that $\tau_{z'z'}-\tau_{y'y'} = -c'\rho k$ and $\tau_{y'z'} = 0$ in the natural coordinates along the isovel and its normal).

This assumption on the principal planes of the stress field is valid near the planes of symmetry. However, it becomes progressively worse away from the planes of symmetry where the major part of the secondary-flow vorticity production takes place. Such evidence may be found in the experimental data obtained by Gessner & Jones (1965) and Perkins (1970). Both sets of experimental data on the Reynolds stresses clearly indicate that the principal planes of the stress field do not lie perpendicular to the isovels inside a triangular sector of the rectangular cross-section.

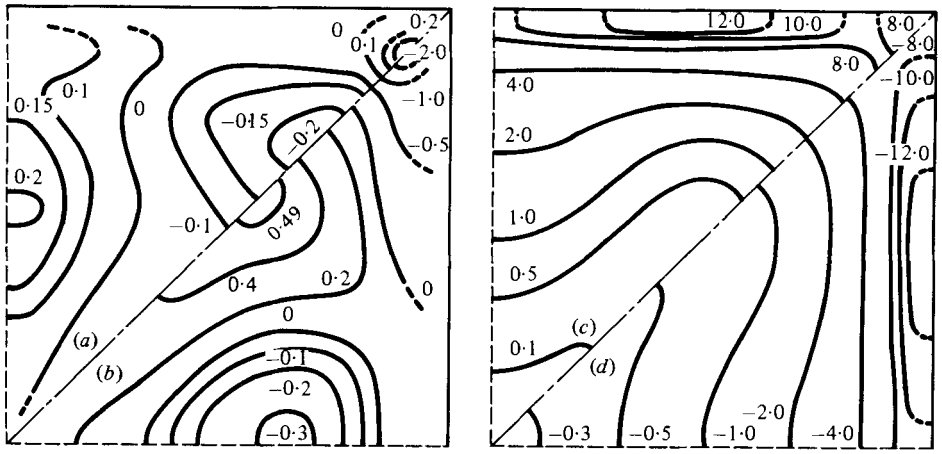

FIGURE 7. Kinetic-energy budget, square duct, present calculation, $Re = 83000$: (*a*) gain rate of convection $[-u_{s_t}(\partial k/\partial s_t)/(u_B^3/D_h)] \times 10^3$; (*b*) gain rate of diffusion $[\nabla . (\Gamma \nabla k)/(u_B^3/D_h)] \times 10^3$; (*c*) gain rate of production $[P/(u_B^3/D_h)] \times 10^3$; (*d*) gain rate of dissipation $[-\epsilon/(u_B^3/D_h)] \times 10^3$.

In order to account for such experimental evidence in the turbulence modelling, a certain effort should be made by way of relaxing the strong requirements imposed on the principal planes of the stress field in conjunction with the isovels. Effort of this kind may eliminate somewhat the unrealistic curvature change observed in $\tau_{zz}-\tau_{yy}$ contours and the sign change observed in τ_{yz} contours, and may eventually lead to an improved version of the stress-and-strain relationship.

3.4. *Transport of kinetic energy in a square duct*

It is of great interest to investigate the details of the kinetic-energy transport process by means of numerical calculation since such details would not be readily available from experiments.

The predicted energy rates plotted in figure 7 are accompanied by signs to indicate energy gain and satisfy

$$\underset{\text{convection}}{[-\bar{\mathbf{u}} . \nabla k]} + \underset{\text{diffusion}}{[\nabla . (\Gamma \nabla k)]} + \underset{\text{production}}{[P]} + \underset{\text{dissipation}}{[-\epsilon]} = 0, \tag{14}$$

where $\bar{\mathbf{u}}$ is the mean-velocity vector.

Observation of the figure reveals the similarity in map patterns between convection and diffusion as well as the similarity between production and dissipation. The figure also indicates that, even away from the wall, the variation of the level of production rate is very similar to that of the dissipation rate. It is obvious from the energy-balance principle that the convection rate must balance with the diffusion rate if the production and the dissipation rates are balanced. Therefore the similarity observed between the convection and diffusion contours may be interpreted as a direct consequence of nearly local equilibrium between the production and the dissipation prevailing throughout the duct (except at the core region, where the production obviously vanishes).

The rates of convection and diffusion are found to be one order of magnitude less than those of production and dissipation. This fact can best be explained by estimating the convection and production terms with the natural coordinates along a secondary-flow streamline. Under this condition, the convection term can be rewritten as

$$-\bar{u} . \nabla k = -u_{s_t} \frac{\partial k}{\partial s_t}, \tag{15}$$

where the secondary-flow magnitude u_{s_t} is always positive when s_t is so chosen. This particular form directly represents the main feature of the convective process, namely that it works against the kinetic-energy gradient in such a way that the kinetic-energy distribution becomes more uniform along the particular streamline.

By virtue of this natural coordinate system, the rate of production along streamlines near the bisectors may also be estimated as

$$P \approx \frac{\tau_{xs_t}}{\rho}\frac{\partial u}{\partial s_t} \quad . \tag{16}$$

The relative magnitude of these two terms may now be estimated with the aid of Townsend's approximation of $\tau_{xs_t}/\rho \approx c_D^{\frac{1}{2}} k$ as

$$\frac{|u_{s_t}\partial k/\partial s_t|}{|c_D^{\frac{1}{2}} k\,\partial u/\partial s_t|} \sim \frac{u_{s_t}}{u_B} c_D^{\frac{1}{2}} \sim 0{\cdot}01 c_D^{-\frac{1}{2}} = \tfrac{1}{30}.$$

The preceding observation already gives a clear overall picture of the energy balance, and the following rough estimation may be made for the region other than the core and corner:

gain rate due to convection $\simeq$ −gain rate due to diffusion,

gain rate due to production $\simeq$ −gain rate due to dissipation,

$$\left|\frac{\text{gain rate due to convection or diffusion}}{\text{gain rate due to production or dissipation}}\right| \approx \tfrac{1}{30}.$$

These energy-budget contours may also be appreciated in conjunction with the predicted kinetic-energy contours already shown in figure 3(*a*). According to (15) it is obvious from this contour map that the gain rate due to convection must be negative as the fluid moves upward along the diagonal from the core, and becomes positive near the corner as $\partial k/\partial s_t$ changes sign from positive to negative. Along the wall bisector, on the other hand, the gain rate due to convection must be positive all the way since $\partial k/\partial s_t$ along the streamline is always negative.

The gain–loss relation of the diffusion term is essentially determined by the local curvature of the kinetic-energy contours since $\nabla.(\Gamma\nabla k) \sim \Gamma\nabla^2 k$. Observation of the predicted kinetic-energy contours along the diagonal reveals the positive curvature changing into a negative one near the corner. Similar observation along the wall bisector from the wall to the core also reveals the change of curvature, which is initially negative and gradually increases to a positive value near the core.

4. Fully developed flow in a rectangular duct

Calculations were performed with the grid system of 14×24 for a quadrant of the rectangular duct of aspect ratio 1:3, for which experimental data of $Re = 56000$ by Leutheusser (1963) and $Re = 30000$ by Hoagland (1960) were available.

4.1. *Mean-velocity field in a rectangular duct*

Isovels normalized by the centreline velocity u_c are shown for $Re = 56000$ in figure 8(*a*), where Leutheusser's experimental data and another prediction with the grid of 12×22 reported by Gosman & Rapley (1980) are also plotted. Both predictions show good agreement with the experiment near the vertical wall bisector, yet overestimate the distortions of isovels toward the corner. Between these two predictions, the velocity-level variations are in fairly good accord except near the

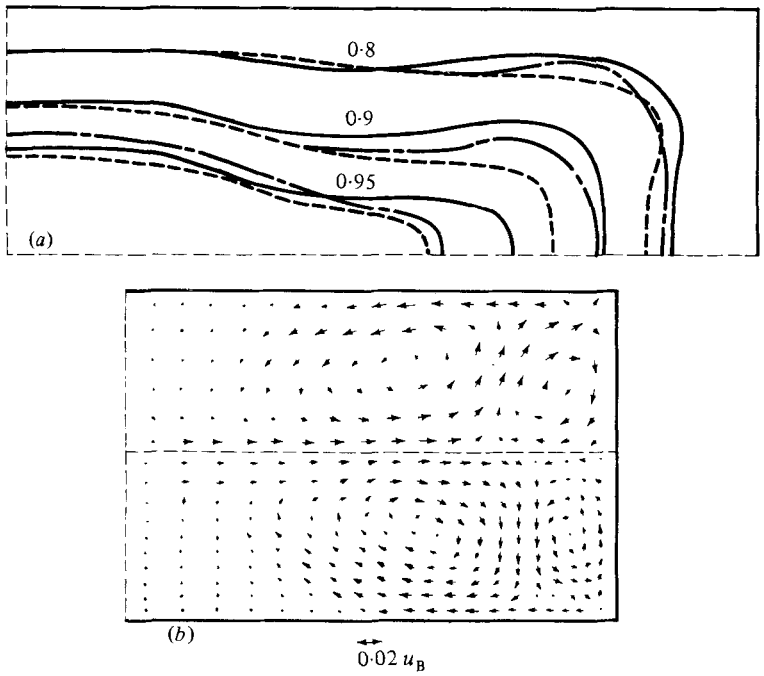

FIGURE 8. Mean-velocity field, rectangular duct (1:3), $Re = 56000$. (*a*) Isovels, u/u_c: ---, experiment (Leutheusser 1963); —·—, calculation (Gosman & Rapley 1980); —, present calculation. (*b*) Secondary-flow velocity vectors: upper half, present calculation; lower half, calculation (Gosman & Rapley 1980).

core. The discrepancy in the velocity levels between two predictions observed near the core should not be taken too seriously since the sensitivity of the isovel location to the velocity magnitude becomes very high as the velocity profile flattens near the core. Closer observation of the predicted contour pattern of Gosman & Rapley with reference to that of the present calculation, however, reveals that the bulge of their contour is directed not toward the corner but somewhat upward toward the wall.

This difference in isovel patterns between the predictions reflects significantly on the secondary-flow patterns as shown in figure 8(*b*). Secondary-flow velocity vectors of Gosman & Rapley indicated in the lower half of the duct seem to direct vertically toward the lower wall before turning to the corner region, while the vectors of the present calculation direct almost diagonally toward the corner as indicated in the other half of the duct. (Some nodes near the sidewall were systematically selected and excluded for a more clear presentation.)

The secondary-flow streamline pattern obtained experimentally by Hoagland (1960), which happens to be the only available information for details of the streamlines in the rectangular duct at this time, is shown in the lower half of figure 9 along with the present calculation in the other half. It presents a trend more favourable to the present velocity-vector distribution rather than that of Gosman & Rapley. The difference in the secondary-flow patterns observed between the two predictions may have been brought out by the different choices of empirical constants and grid systems although both predictions employed essentially the same turbulence models. The most critical empirical constant c', for example, was tuned to be 0·013 in their calculation. This value is about 30 % lower than that employed in the present calculation. Consequently, as observed in figure 8(*b*), the secondary-flow magnitude

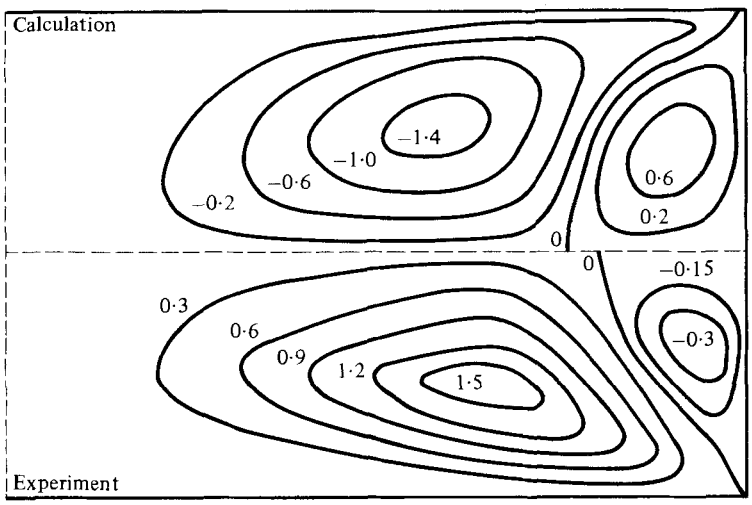

FIGURE 9. Secondary-flow streamlines $[\psi/(u_B D_h)] \times 10^3$, rectangular duct (1:3): upper half, present calculation, $Re = 56000$; lower half, experiment (Hoagland 1960), $Re = 30000$.

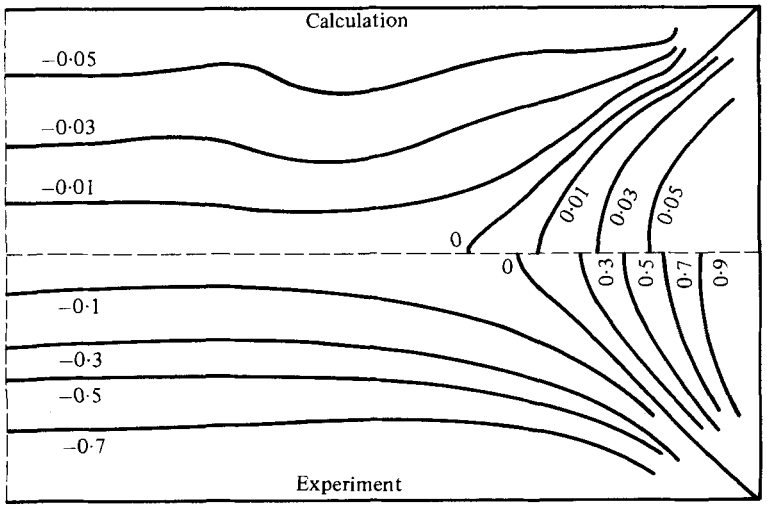

FIGURE 10. Anisotropy of normal stresses $(\tau_{zz} - \tau_{yy})/\tau_{av}$; rectangular duct (1:3): upper half, present calculation, $Re = 56000$; lower half, experiment (Hoagland 1960), $Re = 30000$.

of the present calculation was found to be larger than that of Gosman & Rapley. In addition, the present calculation has 72 nodes more than the grid used by Gosman & Rapley, and they are highly concentrated toward the sidewall in order to resolve the adjacent vortex.

4.2. *Anisotropy of normal stresses in a rectangular duct*

The anisotropy of normal stresses is indicated in figure 10 along with the experimental data of Hoagland (1960). The predicted pattern shows similar contours with the experimental data although the level is again underpredicted to one order of magnitude less than that of the experiment. Bulges on the predicted contour lines in the upper trapezoidal sector may also be found near the locations of the inflexion points along the isovels already shown in figure 8(*a*).

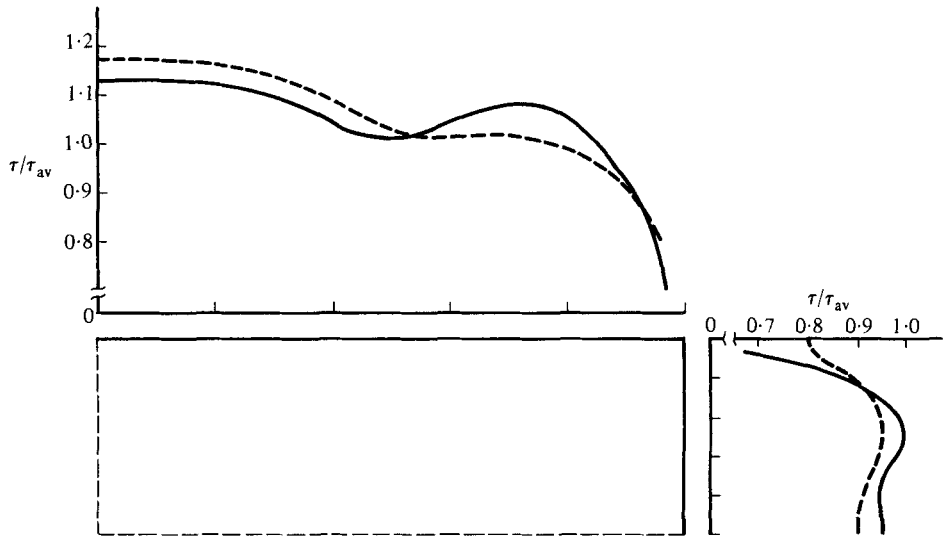

FIGURE 11. Wall-shear distribution τ/τ_{av}; rectangular duct (1:3); $Re = 56000$: ---, experiment (Leutheusser 1963); —, present calculation.

4.3. *Wall-shear distribution in a rectangular duct*

The predicted wall-shear distribution normalized by its average value over the periphery is shown in figure 11 along with the experimental data of Leutheusser (1963). Along the upper wall the prediction underestimates the wall shear near the wall bisector and overestimates it near the corner. The relative difference between the upper and sidewall shears, however, is in fairly good accord with that of the experiment.

5. Fully developed flow in a trapezoidal duct

An attempt was also made to calculate the fully developed turbulent flow in a trapezoidal duct for which no predictions were reported. A non-orthogonal coordinate system with a 14×27 grid was employed for one-half the trapezoidal duct with corner angles of 75° and 105° $Re = 240000$. Results of calculations were compared with the experimental data by Rodet (1960).

5.1. *Mean-velocity field in a trapezoidal duct*

The predicted isovels are plotted along with the experimental data in figure 12(*a*). The prediction shows good agreement with the experiment except at the region near the corner with an acute angle where the prediction underestimates the velocity level.

The predicted secondary-flow vectors are shown in figure 12(*b*). The figure indicates a big vortex surrounded by three smaller vortices. The vortex size may be estimated from the isovel pattern in figure 12(*a*) according to Prandtl's (1926) suggestion, namely the secondary flow away from the core is directed toward the corner through the region of convex isovels, and then returns to the core through the region of concave isovels. Both experimental and predicted isovels in figure 12(*a*) indicate a secondary-flow pattern similar to the one actually observed in figure 12(*b*).

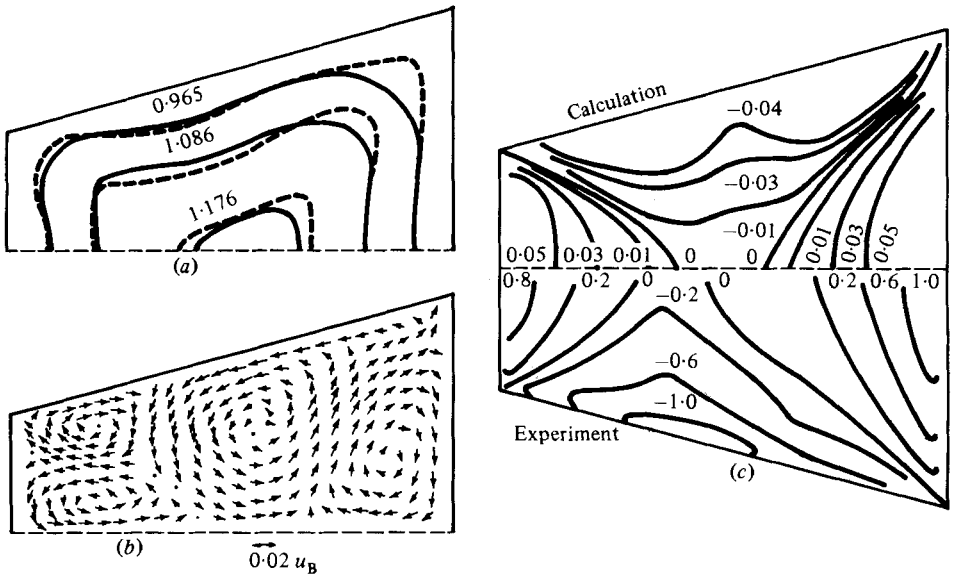

FIGURE 12. Mean-velocity field and anisotropy of normal stresses, trapezoidal duct (corner angles 75° and 105°), $Re = 240000$. (*a*) Isovels u/u_B: ---, experiment (Rodet 1960); —, present calculation. (*b*) Secondary-flow velocity vectors, present calculation. (*c*) $(\tau_{zz}-\tau_{yy})/\tau_{av}$: upper half, present calculation; lower half, experiment (Rodet 1960).

5.2. *Anisotropy of normal stresses in a trapezoidal duct*

The anisotropy of normal stresses is shown along with the experimental data in figure 12 (*c*). Similar comments already given for square and rectangular ducts may be made for this figure. The distortion of contour lines near the upper wall appears only at the middle of the contour line.

5.3. *Wall-shear distribution in a trapezoidal duct*

The wall-shear distribution is indicated in figure 13. The damping effect of the duct corner on the wall-shear distribution becomes more effective for the corner with an acute angle. This may be explained by the fact that interferences of the walls to the normal stresses are naturally more significant for the walls intersecting at a smaller angle.

6. Friction coefficients of non-circular ducts

The predicted friction coefficients $C_f = 2\tau_{av}/\rho u_B^2$ of the square, rectangular and trapezoidal ducts are plotted together in figure 14. The square-duct prediction by Launder & Ying (1973) based on a one-equation model, and their results obtained by suppressing the secondary-flow motion, are also shown along with experimental data obtained by various workers (Leutheusser 1963; Launder & Ying 1972; Hartnett, Koh & McDomas 1962). The present prediction gives better agreement with most of the experimental data. Clearly, suppression of the secondary-flow motion leads to gross errors from underestimating the friction coefficient.

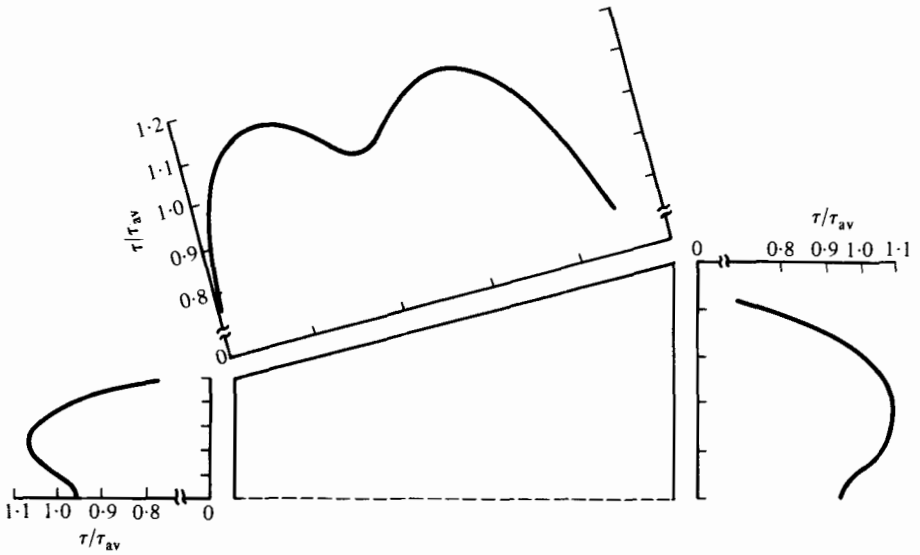

FIGURE 13. Wall-shear distribution τ/τ_{av}, trapezoidal duct (corner angles 75° and 105°): present calculation, $Re = 240000$.

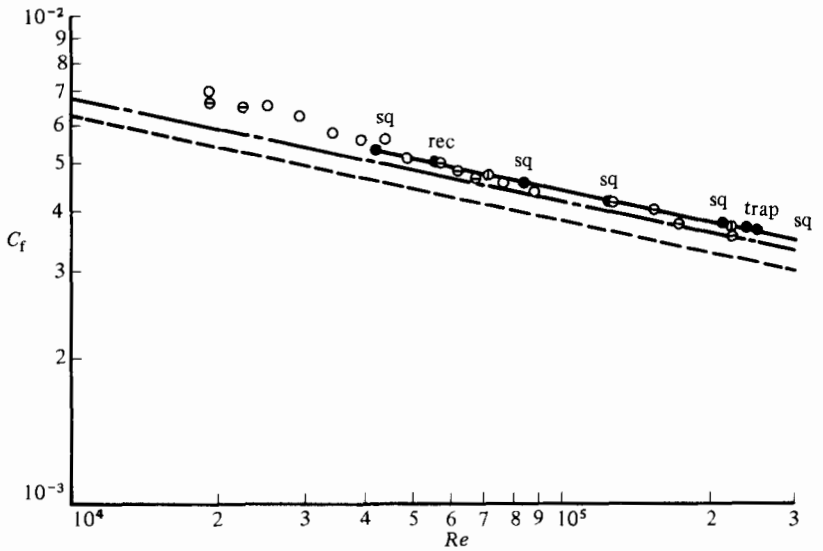

FIGURE 14. Friction coefficients C_f in non-circular ducts: ○, experiment (Leutheusser 1963); ⊕, experiment (Launder & Ying 1972); ⊖, experiment (Harnett *et al.* (1962); – – –, calculation without secondary flow (Launder & Ying 1973); —·—, calculation with secondary flow (Launder & Ying 1973); —●—, present calculation (sq, square; rec, rectangle; trap, trapezoid).

7. Conclusions

The algebraic stress model, when coupled with the k and ϵ model, leads to reasonably satisfactory predictions on the mean-velocity fields in non-circular ducts. The model performance on the Reynolds stress fields, however, is by no means satisfactory when compared with the experimental data. The anisotropy of normal stresses and the secondary shear stress acting in the cross-sectional plane, the gradients of which are major causes of the secondary-flow motions, are underestimated to one order of magnitude less than the experimental data.

The level of friction coefficients of non-circular ducts predicted by the algebraic stress model is higher than that obtained without secondary-flow effects and appears to be in good agreement with the experimental data.

This work was partially supported by the U.S. Army Research Office through Research Grant no. DAAG 29-79-C-0184.

Appendix. Coordinate transformation

The transformation for the fully developed flows may be given in the general form of

$$x = \xi, \quad y = y(\eta, \zeta), \quad z = z(\eta, \zeta). \qquad \text{(A 1, A 2, A 3)}$$

From the above equations, the general conservation equation (1) may be transformed into an arbitrary system of coordinates (ξ, η, ζ) as

$$[J(\mathbf{d}_2 \cdot \mathbf{u})\,\phi - J\Gamma \mathbf{d}_2^2 \phi_\eta]_\eta + [J(\mathbf{d}_3 \cdot \mathbf{u})\,\phi - J\Gamma \mathbf{d}_3^2 \phi_\zeta]_\zeta = s_\phi^*, \qquad \text{(A 4)}$$

where

$$\mathbf{u} = u\mathbf{i} + v\mathbf{j} + w\mathbf{k}, \qquad \text{(A 5)}$$

$$s_\phi^* = J s_\phi + [J\Gamma(\mathbf{d}_2 \cdot \mathbf{d}_3)\,\phi_\zeta]_\eta + [J\Gamma(\mathbf{d}_2 \cdot \mathbf{d}_3)\,\phi_\eta]_\zeta, \qquad \text{(A 6)}$$

$$\mathbf{d}_1 = \mathbf{i}, \quad \mathbf{d}_2 = (z_\zeta \mathbf{j} - y_\zeta \mathbf{k})J, \quad \mathbf{d}_3 = (-z_\eta \mathbf{j} + y_\eta \mathbf{k})J^{-1}, \qquad \text{(A 7, A 8)}$$

$$J = (\mathbf{d}_1 \cdot \mathbf{d}_2 \times \mathbf{d}_3)^{-1} = y_\eta z_\zeta - y_\zeta z_\eta. \qquad \text{(A 9)}$$

Here $\mathbf{i}$, $\mathbf{j}$ and $\mathbf{k}$ are unit vectors in the x-, y- and z-directions respectively. The subscripts ξ, η and ζ as usual denote partial derivatives. J is the Jacobian of the transformation.

It should be noted that $\mathbf{u}$ is to take u, v and w (in the Cartesian frame) as components even in the new coordinate system (ξ, η, ζ). Naturally, each of these velocity components remains as the dependent variable ϕ in the corresponding momentum equation (thus the terms corresponding to the Christoffel symbols in a general tensor notation do not appear in the present momentum equations).

The general finite-difference form obtained through the discretization of the general conservation equation (A 4), is so universal that it can be used for any coordinates simply by specifying $\mathbf{d}_2$ and $\mathbf{d}_3$ or equivalently $y(\eta, \zeta)$ and $z(\eta, \zeta)$. For the present study, the following transformation was found to be adequate:

$$y = Y_b + (Y_t - Y_b)\,\eta, \quad z = \zeta, \qquad \text{(A 10, A 11)}$$

where Y_b and Y_t represent respectively the lower- and upper-wall geometries, are functions of ζ alone. Consequently η varies from zero to unity.

REFERENCES

Aly, A. M. M., Trupp, A. C. & Gerrard, A. D. 1978 Measurements and prediction of fully developed turbulent flow in an equilateral triangular duct. *J. Fluid Mech.* **85**, 57–83.

Brundrett, E. & Baines, W. D. 1964 Production and diffusion of vorticity in duct flow. *J. Fluid Mech.* **19**, 375–394.

Carajilescov, P. & Todreas, N. E. 1975 Experimental and analytical study of axial turbulent flows in an interior subchannel of a bare rod bundle. *Transl A.S.M.E.* C: *J. Heat Transfer* **98**, 262–268.

Gessner, F. B. & Emery, A. F. 1976 A Reynolds stress model for turbulent corner flows – part I: development of the model. *Trans. A.S.M.E.* I: *J. Fluid Engng* **98**, 261–268.

GESSNER, F. B. & JONES, J. B. 1965 On some aspects of fully developed turbulent flow in rectangular channels. *J. Fluid Mech.* **23**, 689–713.

GOSMAN, A. D. & RAPLEY, C. W. 1978 A prediction method for fully developed flow through non-circular passages. In *Proc. 1st Intl Conf. on Num. Methods in Laminar and Turbulent flow, University College Swansea*, pp. 271–285.

GOSMAN, A. D. & RAPLEY, C. W. 1980 Fully developed flow in passages of arbitrary cross-section. *Recent Advances in Numerical Methods in Fluids* vol. 1 (ed. C. Taylor & K. Morgan), pp. 335–399. Pineridge.

HARTNETT, J. P., KOH, J. C. & MCDOMAS, S. 1962 A comparison of predicted and measured friction factors for flow through rectangular ducts. *Trans. A.S.M.E.* C: *J. Heat Transfer* **84**, 82–88.

HOAGLAND, L. C. 1960 Fully developed turbulent flow in straight rectangular ducts. Ph.D. thesis, M.I.T.

LAUNDER, B. E. 1976 Discussion on Gessner and Emery's work (1976). *Trans. A.S.M.E.* I: *J. Fluids Engng* **98**, 276–277.

LAUNDER, B. E. & YING, W. M. 1972 Secondary flows in ducts of square cross-section. *J. Fluid Mech.* **54**, 289–295.

LAUNDER, B. E. & YING, W. M. 1973 Prediction of flow and heat transfer in ducts of square cross-section. *Heat Fluid Flow* **3**, No. 2, 115–121.

LEUTHEUSSER, H. J. 1963 Turbulent flow in rectangular ducts. *J. Hydraul. Div. A.S.C.E.* **89** (HY3), 1–19.

MELLING, A. & WHITELAW, J. H. 1976 Turbulent flow in a rectangular duct. *J. Fluid Mech.* **78**, 289–315.

NAKAYAMA, A. 1981 Three-dimensional flow within conduits of arbitrary geometrical configurations. Ph.D. thesis, University of Illinois at U–C.

NAKAYAMA, A., CHOW, W. L. & SHARMA, D. 1981 Summary submitted for the 1980–81 AFOSR-HTTM-Stanford Conf. on Complex Turbulent Flows: Comparison to Computation and Experiment. (To be published in conference proceedings.)

NIKURADSE, J. 1926 Untersuchung über die Geschwindigkeitsverteilung in turbulenten Strömungen. Diss. Göttingen, *VDI-forschungsheft* 281.

NIKURADSE, J. 1930 Untersuchungen über turbulente Strömungen in nicht kreisformigen Rohren. *Ing.-Archiv* **1**, 306–332.

PATANKAR, S. V. & SPALDING, D. B. 1972 A calculation procedure for heat, mass, and momentum transfer in three-dimensional parabolic flows. *Int. J. Heat Mass Transfer* **15**, 1787–1805.

PERKINS, H. J. 1970 The formation of streamwise vorticity in turbulent flow. *J. Fluid Mech.* **44**, 721–740.

PRANDTL, L. 1926 Über die ausgebildete Turbulenz. In *Proc. 2nd Int. Kong. für Tech. Mech., Zürich* (transl. *NACA Tech. Memo* no. 435).

RODET, E. 1960 Etude de l'écoulement d'un fluide dans un tunnel prismatique de section trapézoïdale. *Publ. Sci. et Tech. du Min. de l'Air*, no. 369.